Synthesis and characterizations of highly conductive and stable electrolyte Li$_{10}$P$_3$S$_{12}$I

Xuyong Feng [a],[1], Po-Hsiu Chien [a],[1], Sawankumar Patel [a], Jin Zheng [a], Marcello Immediato-Scuotto [a], Yan Xin [b], Ivan Hung [c], Zhehong Gan [c], Yan-Yan Hu [a],[c],[*]

[a] Department of Chemistry and Biochemistry, Florida State University, Tallahassee, FL, 32306, USA
[b] Magnet Science and Technology, National High Magnetic Field Laboratory, 1800 East Paul Dirac Drive, Tallahassee, FL, 32310, USA
[c] Center of Interdisciplinary Magnetic Resonance, National High Magnetic Field Laboratory, 1800 East Paul Dirac Drive, Tallahassee, FL, 32310, USA

ARTICLE INFO

ABSTRACT

A novel glass-ceramic solid electrolyte Li$_{10}$P$_3$S$_{12}$I is synthesized, which delivers a high ionic conductivity of 6.4 mS/cm at 25 °C and a low activation energy of 0.26 eV. Li$_{10}$P$_3$S$_{12}$I also exhibits significantly enhanced stability and low interfacial resistance against Li metal compared with thiophosphates. Tracer-exchange Li NMR reveals that lithium ions transport preferably through the glass phase and glass-ceramic interface in Li$_{10}$P$_3$S$_{12}$I. Careful control of the synthesis process to avoid complete crystallization helps stabilize the highly Li-conductive phase.

1. Introduction

All-solid-state rechargeable batteries are quickly rising to prominence due to their enhanced safety, high energy density, and improved stability [1–3]. The characteristics of high-performance solid electrolytes are high ionic conductivity, electrode-compatibility with low interfacial resistance, favorable mechanical properties, and good electrochemical/chemical stability. Ionic conductivities on the order of mS/cm have been achieved in several solid electrolytes such as Li$_6$PS$_5$Cl [4–8], Li$_7$La$_3$Zr$_2$O$_{12}$ [9–11], Li$_{1.3}$Al$_{0.3}$Ti$_{1.7}$(PO$_4$)$_3$ [12,13], and Li$_3$ClO [14]. Although an ionic conductivity of 1 mS/cm is acceptable for practical applications, all-solid-state batteries aiming for high power densities require higher ionic conductivity. Up to now, only a few solid electrolytes including Li$_{10}$GeP$_2$S$_{12}$ and its analogues [15–17], Li$_7$P$_3$S$_{11}$ [18], and Ge-doped Li$_6$PS$_5$I [19], can reach an ionic conductivity over 5 mS/cm at room-temperature. However, the high cost of Ge limits large-scale applications of Ge-containing electrolytes [16,20]. For Li$_7$P$_3$S$_{11}$, hot-press is necessary to achieve ionic conductivity over 5 mS/cm, which increases manufacturing cost. In addition, the instability of Li$_{10}$GeP$_2$S$_{12}$ and Li$_7$P$_3$S$_{11}$ against Li metal makes them less appealing as solid electrolytes for high-performance solid-state lithium batteries.

Most lithium thiophosphates decompose to Li$_2$S, Li$_3$P, and other components when they are in contact with Li metal [17,21–23]. The formation of self-limiting solid-electrolyte-interphases (SEIs) can restrict detrimental side reactions [21,24]. Therefore, the strategy to improve the interfacial stability is to introduce ionically conductive but electronically insulating SEI species in situ or ex situ. For Li$_{10}$GeP$_2$S$_{12}$, ex-situ approaches often employ surface coating such as LiNbO$_3$ on electrodes [15], LiH$_2$PO$_4$ on Li metal [20], or polyethylene oxide on Li$_{10}$GeP$_2$S$_{12}$ [25]. Surface modifications prove to enhance the stability, but pay the price with increased interfacial resistance. Furthermore, thin coating layers are prone to breakdown due to interfacial side reactions over long-term cycling. Among lithium thiophosphate derivatives, Li$_7$P$_2$S$_8$I shows significantly improved stability against lithium metal [26]. Han et al. reported that incorporating LiI into Li$_2$S–P$_2$S$_5$ solid electrolytes can suppress lithium dendrite formation and improve the chemical and electrochemical stability [27]. Although Li$_7$P$_2$S$_8$I possesses good stability, the ionic conductivity often prepared with a solution-based method is reported lower than 1 mS/cm [28,29]. In this paper, we demonstrate a different synthesis approach for preparing glass-ceramic Li$_{10}$P$_3$S$_{12}$I at a low temperature of 230 °C. The achieved ionic conductivity of the Li$_{10}$P$_3$S$_{12}$I pellets prepared with cold-press is 6.4 mS/cm at 25 °C with an activation energy of 0.26 eV. Li-ion transport in Li$_{10}$P$_3$S$_{12}$I is determined to be mainly through the disordered phases, especially glass-ceramic interface. Li$_{10}$P$_3$S$_{12}$I shows significantly enhanced stability against Li metal as compared with lithium thiophosphates and low interfacial

---

resistance.

2. Material and methods

2.1. Preparation of $Li_{10}P_3S_{12}I$

The glass-ceramic $Li_{10}P_3S_{12}I$ electrolytes were prepared via solid-state reactions. The chemicals were purchased from Sigma-Aldrich and used without further purifications. Li_2S, P_2S_5, and LiI were weighed with a molar ratio of $Li_2S : P_2S_5 : LiI = 9 : 3 : 2$ in an Ar-filled glovebox (Mbraun Inc.). The mixed precursors were added into a 25 mL ZrO_2 jar with two 10-mm ZrO_2 balls. The raw materials were sealed in the jar under vacuum and ball-milled for 10 h using a SPEX SamplePrep 8000 M mixer. After ball milling, the mixtures were sintered at 230 °C for 1 h under Ar in a quartz tube followed by pressing into pellets with a diameter of 6 mm and a thickness of 1 mm under 1000 MPa in Ar-filled glovebox. $Li_7P_3S_{11}$ was synthesized according to the literature [30].

2.2. Materials characterizations

Differential scanning calorimetry (DSC) was performed using TA Q100 with a heating rate of 10 °C/min under Argon. Powder X-ray diffraction (XRD) experiments were performed at room temperature on a Philips X'Pert powder X-ray diffractometer using a Cu-Kα1 radiation ($\lambda = 1.5406$ Å). SEM images were acquired on a NOVA NanoSEM 400 field-emission scanning electron microscopy. TEM images were acquired using a JEM-ARM200cF. ^6Li and ^7Li magic-angle-spinning (MAS) NMR spectra were acquired on a Bruker Avance-III 500 spectrometer with a Bruker 2.5-mm HXY probe spinning at 25 kHz. A single-pulse sequence was employed for $^{6,7}Li$ NMR measurements. For ^6Li NMR, a solid $\pi/2$ pulse length of 4.75 µs and a recycle delay of 500 s were used. For ^7Li NMR, a solid $\pi/2$ pulse length was 0.6 µs and a recycle delay was 50 s. $^{6,7}Li$ spectra were referenced to $LiCl_{(s)}$ at 0 ppm. ^{127}I magic-angle-spinning (MAS) NMR experiments were carried out on a Bruker Avance NEO spectrometer at 19.6 T using a National High Magnetic Field Laboratory built 3.2-mm probe spinning at 16 kHz [31]. A rotor-synchronized Hahn echo pulse sequence was employed with a solid $\pi/2$ pulse length of 1.32 µs and a recycle delay of 1 s. The ^{127}I Multiple-Quantum MAS (MQMAS) spectrum of $Li_{10}P_3S_{12}I$ was acquired using a shifted echo sequence with a recycle delay of 0.02 s. 9600 scans for each rotor-synchronized t_1 increment (32 in total) were acquired. ^{127}I spectra were referenced to 0.1 M $KI_{(aq)}$ at 0 ppm. All solid-state NMR spectra were analyzed and processed using Topspin (v3.2) and Dmfit (#20180327). The conductivities were determined with AC impedance spectroscopy. Indium foil was pressed to both sides of the electrolyte pellets. The electrochemical impedance spectroscopy (EIS) was performed using a Gamry Reference 600+ between frequencies of 5 MHz to 1 Hz with an amplitude of 20 mV in the temperature range of −60 to 120 °C. The conductivity was calculated based on the resistance obtained from analyzing the impedance spectra using equivalent circuits. Cyclic voltammetry was employed on $Li/Li_{10}P_3S_{12}I$/stainless steel cell, with a scan rate of 5 mV/s and voltage range of −0.3 - 3.0 V. Electrochemical stability against Li metal was measured in symmetric $Li/Li_{10}P_3S_{12}I$ or $Li_7P_3S_{11}/Li$ cells with different current densities. In both EIS and electrochemical stability tests, the diameter and the thickness of the $Li_{10}P_3S_{12}I$ pellet is 6 mm and 1 mm, respectively. The In or Li foil used is 5 mm in diameter, which is used for calculating the surface area $(2.5 \text{ mm} \times 2.5 \text{ mm} \times \pi)$.

3. Results and discussion

3.1. Structural characterizations of $Li_{10}P_3S_{12}I$

According to the DSC result (Fig. S1), the pristine powder underwent two exothermic processes (203 °C and 269 °C) when heated up to 300 °C. The process at about 203 °C corresponds to crystallization of the low-temperature $Li_{10}P_3S_{12}I$ phase and the process at about 269 °C corresponds to crystallization of the high-temperature $Li_{10}P_3S_{12}I$ phase [32]. Structural characterizations are carried out with powder X-ray diffraction (PXRD), transmission electron microscopy (TEM), and solid-state Li NMR. The PXRD pattern of $Li_{10}P_3S_{12}I$ is shown in Fig. S2, in which the weak and broad diffraction peaks suggest the existence of nanocrystalline particles. The two diffraction peaks at around 21° and 28° indicate the poorly crystallized phase adapts a similar structure as previously reported LPSI compounds [26]. The other two peaks at about 20° and 29.6° are ascribed to diffraction from the low-temperature $Li_{10}P_3S_{12}I$ phase [32,33]. The broad diffraction peaks underneath suggest phases with significant structural disorder. The glass-ceramic nature of $Li_{10}P_3S_{12}I$ is be further confirmed with TEM and selected area electronic diffraction (SEAD) shown in Fig. 1. As seen in TEM, $Li_{10}P_3S_{12}I$ is composed of a glass matrix with nanocrystals embedded in it. The size of the nanocrystals is between 5 and 15 nm. The SEAD (Fig. 1d) also confirms the co-existence of nanocrystals and the glass matrix.

Structural features with short-range ordering are difficult to extract from XRD or TEM. Therefore, high-resolution solid-state NMR is employed to probe the disordered phases. ^6Li, ^7Li, and ^{127}I NMR spectra of $Li_{10}P_3S_{12}I$ are presented in Fig. 2a, c, and 2d. ^6Li NMR shows one single resonance at 1.5 ppm, which is distinctive from that for Li_3PS_4 (2 ppm) or crystalline $Li_7P_2P_8I$ (0.84 ppm). $Li_{6+x}P_2S_8I_x$ $(0 < x < 2)$ shows ^7Li shifts between 0.8 and 2.2 ppm and the shift decreases linearly with the x value in $Li_{6+x}P_2S_8I_x$ $(0 < x < 2)$ (Fig. 2b and Fig. S3). Based on the established linear correlation, the single resonance at 1.5 ppm shown in Fig. 1a corresponds to $x = 0.67$ in $Li_{6+x}P_2S_8I_x$, i.e., $Li_{10}P_3S_{12}I$. ^7Li T_1 NMR relaxation time for $Li_{10}P_3S_{12}I$ is determined as 0.86 s, which is similar to the T_1 time for $Li_{10}GeP_2S_{12}$ (0.23 s) and suggests fast Li ion motion. ^{127}I NMR on $Li_{10}P_3S_{12}I$ has also been acquired (Fig. 2d), which shows a resonance centered around 105 ppm. All the LiI participates to form the new phase $Li_{10}P_3S_{12}I$ as implied by the absence of both the signature peaks for LiI at −3.4 ppm in the ^6Li NMR (Fig. 2c) and at 390 ppm in the ^{127}I NMR. In summary, NMR characterizations confirm the composition of $Li_{10}P_3S_{12}I$ and suggest fast Li-ion motion.
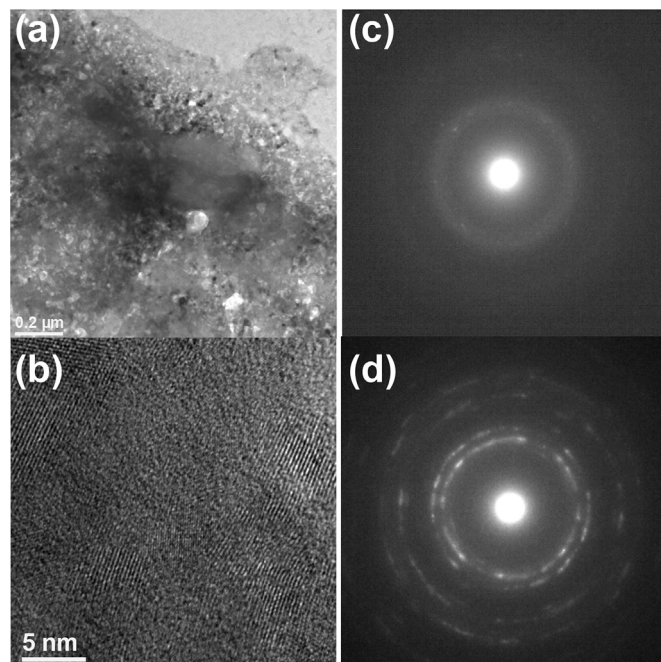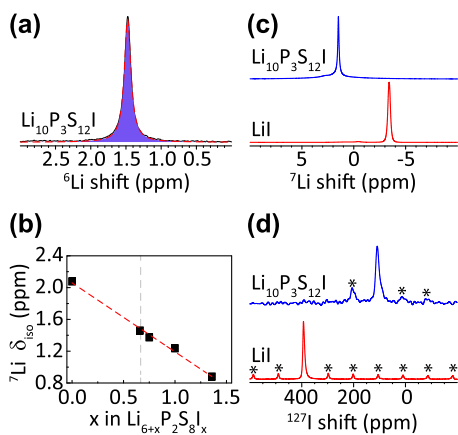

Fig. 1. (a) TEM bright field image of $Li_{10}P_3S_{12}I$ containing glass and crystallized region. (b) HRTEM image showing nanocrystals with the size of 5–15 nm imbedded in an amorphous matrix (c) Selected area diffraction pattern from amorphous region showing typical amorphous diffraction ring. (d) Selected area diffraction pattern of the region containing nanocrystals.

Fig. 2. (a) ^{6}Li NMR of $Li_{10}P_3S_{12}I$. (b) The linear correlation of ^{7}Li chemical shift vs. x in $Li_{6+x}P_2S_8I_x$ ($0 < x < 2$). (c) ^{7}Li NMR of $Li_{10}P_3S_{12}I$ and LiI. (d) ^{127}I NMR of $Li_{10}P_3S_{12}I$ and LiI.

3.2. Ionic conductivity and chemical stability (vs. Li metal) test

The ionic conductivity of $Li_{10}P_3S_{12}I$ is determined by variable-temperature AC impedance measurements. The selective impedance spectra between $-60\,°C$ to $120\,°C$ are presented in the inset of Fig. 3. The calculated ionic conductivity σ based on impedance measurements is plotted as a function of temperature (Fig. 3). The activation energy is determined as 0.26 eV from the slope of the Arrhenius plot, log σ vs. $1000/T$ (Fig. 3). The ionic conductivity at $25\,°C$ is 6.4 mS/cm. $Li_{10}P_3S_{12}I$ is among the most highly conductive Li solid electrolytes (Fig. 4a), which only has slightly lower ionic conductivity than $Li_{10}GeP_2S_{12}$, hot-pressed $Li_7P_3S_{11}$, and sintered Ge-doped Li_6PS_5I. The fabrication of the $Li_{10}P_3S_{12}I$ pellet does not involve hot-press as for $Li_7P_3S_{11}$. The cold-pressed $Li_{10}P_3S_{12}I$ pellet shows smooth surface (Fig. S5a) and low porosity from cross-section view (Fig. S5b), which contributes to the high conductivity. Furthermore, compared with $Li_{10}GeP_2S_{12}$ and $Li_7P_3S_{11}$, $Li_{10}P_3S_{12}I$ demonstrates much better stability against Li metal. As shown in Fig. 4b, with a current density of $0.2\,mA/cm^2$, $Li/Li_{10}P_3S_{12}I/Li$ shows very stable voltage profile over an extended time, while $Li/Li_7P_3S_{11}/Li$ exhibits continuously increased voltage with significant instability and short-circuit within 65 h (Fig. S7). The critical current density for $Li/Li_{10}P_3S_{12}I/Li$ is determined as $0.6\,mA/cm^2$ (Fig. S6), which is expected to significantly improve with interface processing. $Li/Li_{10}P_3S_{12}I/Li$ also shows very low interfacial resistance between $Li_{10}P_3S_{12}I$ and Li, which is only about $7\,Ω{*}cm^2$ (Fig. S8). Cyclic voltammetry measurement shown in Fig. S9 reveals the stability of $Li_{10}P_3S_{12}I$ up to 5 V, no other reactions occur from -0.3–5 V except the deposition and dissolution of Li on the stainless steel.

3.3. Determination of ion transport pathways in $Li_{10}P_3S_{12}I$

To understand the source of high ionic conductivity found in $Li_{10}P_3S_{12}I$, ^{6}Li → ^{7}Li tracer-exchange NMR experiments have been performed using a ^{6}Li | ^{7}Li$_{10}$P$_3$S$_{12}$I | ^{6}Li symmetric cell to probe the Li-ion transport pathways [39]. After the ^{6}Li → ^{7}Li tracer-exchange driven by a biased electric potential, ^{6}Li partially replaces ^{7}Li in $Li_{10}P_3S_{12}I$ on the pathways. By identifying which structural Li goes through the ^{6}Li → ^{7}Li tracer-exchange with high-resolution ^{7}Li and ^{6}Li NMR, functional Li sites responsible for fast Li-ion transport can be determined. Minor decomposition products due to the electrochemical cycling are also studied at the same time. The comparison of ^{6}Li NMR spectra on $Li_{10}P_3S_{12}I$ before and after ^{6}Li → ^{7}Li tracer-exchange is shown in Fig. 5, with the difference spectrum plotted in green. It is worth mentioning that the ^{7}Li (spin-3/2) NMR line-shape is characterized by a narrow peak corresponding to central transition superimposed on a broad low-intensity component
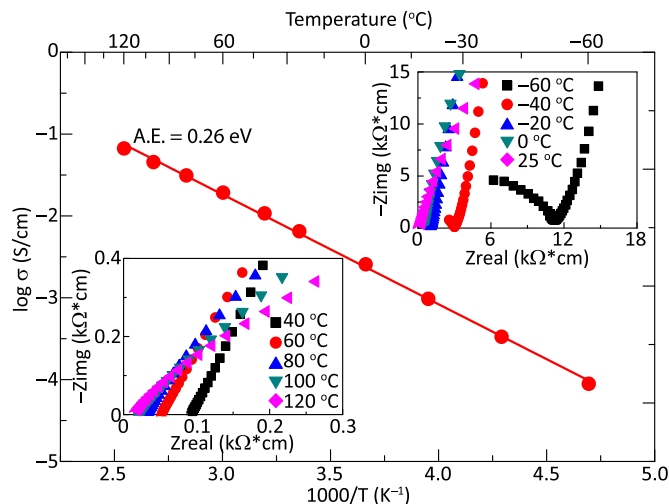

Fig. 3. Arrhenius plot showing the ionic conductivity as a function of temperature for $Li_{10}P_3S_{12}I$. The insets show the variable-temperature Nyquist plots of the impedance as a function of temperature for $Li_{10}P_3S_{12}I$ from $-60\,°C$ to $120\,°C$.
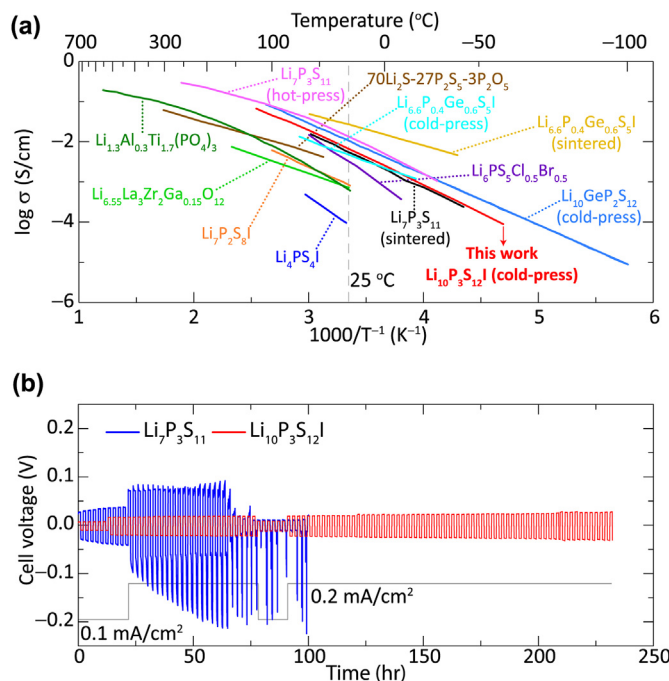
Fig. 4. Electrochemical properties of $Li_{10}P_3S_{12}I$. (a) Arrhenius plots of lithium thiophosphate solid electrolytes. Oxide-based lithium solid electrolytes with high ionic conductivities are also shown for comparison ($Li_{1.3}Al_{0.3}Ti_{1.7}(PO_4)_3$ [34], $Li_{6.55}La_3Zr_2Ga_{0.15}O_{12}$ [35], $Li_{6.6}P_{0.4}Ge_{0.6}S_5I$ [19], $Li_6PS_5Cl_{0.5}Br_{0.5}$ [36], $70Li_2S·27P_2S_5·3P_2O_5$ [37], Li_4PS_4I [38], $Li_7P_3S_{11}$ (hot press) [18], $Li_7P_3S_{11}$ [30], $Li_{10}GeP_2S_{12}$ [15], $Li_7P_2S_8I$ [26]). Fabrication difference is given in parentheses. (b) Galvanic cycling of $Li/Li_{10}P_3S_{12}I/Li$ and $Li/Li_7P_3S_{11}/Li$ at $21\,°C$.

corresponding to the satellite transitions. ^{7}Li NMR (Fig. S10a) reveals significant decrease in the major resonance from $Li_{10}P_3S_{12}I$ at 1.5 ppm, which corresponds to the increase of the same $Li_{10}P_3S_{12}I$ resonance in ^{6}Li NMR (Fig. 5a), suggesting that ^{6}Li → ^{7}Li tracer-exchange occurs in $Li_{10}P_3S_{12}I$. In addition, a broad ^{6}Li resonance centered at 1.5 ppm appears after electrochemical tracer-exchange with significant sensitivity enhancement. This resonance originates from more disordered interface within the glass-ceramic $Li_{10}P_3S_{12}I$.

Detailed analysis of the ^{7}Li and ^{6}Li NMR spectra after tracer-exchange
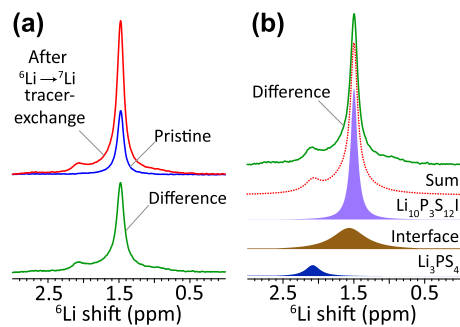
Fig. 5. $^6Li \rightarrow {}^7Li$ tracer-exchange NMR probes Li ion transport pathways in $Li_{10}P_3S_{12}I$. (a) ^6Li NMR spectra of $Li_{10}P_3S_{12}I$ before and after $^6Li \rightarrow {}^7Li$ tracer-exchange, and the difference spectrum (red line – blue line). (b) Simulation of the difference ^6Li NMR spectrum shown in (a). (For interpretation of the references to colour in this figure legend, the reader is referred to the Web version of this article.)

are shown in Fig. 5b and Fig. S10. ^7Li NMR reveals that 78% of ^7Li is from $Li_{10}P_3S_{12}I$, 17% from the glass-ceramic interface, and 5% from the minor decomposition product Li_3PS_4. While ^6Li NMR shows that 60% of ^6Li resides in $Li_{10}P_3S_{12}I$, 35% in the glass-ceramic interface, and 5% in Li_3PS_4. If Li were to travel equally through both $Li_{10}P_3S_{12}I$ phase and glass-ceramic interface, the $^6Li \rightarrow {}^7Li$ tracer-exchange in both phases should be similar. Thus, the phase composition detected in ^7Li and ^6Li NMR should be very close. The enhanced fraction of the glass-ceramic interface in ^6Li NMR compared with that in ^7Li NMR suggests that Li prefers to transport through the glass-ceramic interface. The high-resolution ^7Li and ^6Li NMR on $Li_{10}P_3S_{12}I$ before and after the electrochemical $^6Li \rightarrow {}^7Li$ tracer-exchange consistently reveal that Li conduction is through $Li_{10}P_3S_{12}I$ with a preference to the glass-ceramic interface. Also, minor decomposition occurs to form Li_3PS_4, in which the final by-product should be LiI; the in situ formed LiI helps to stabilize the Li–$Li_{10}P_3S_{12}I$ interface [27]. The decomposition of $Li_{10}P_3S_{12}I$ at the Li-electrolyte interface slightly increases the overall voltage as observed in Fig. 4b. Further impedance measurements shown in Fig. S8 reveal that the overall voltage increase is attributed to the rise of interfacial resistance from 7 $\Omega*cm^2$ to 20 $\Omega*cm^2$. However, as the decomposition is self-limiting, the voltages stabilizes very quickly and stays low.

4. Conclusions

In summary, the $Li_{10}P_3S_{12}I$ electrolyte is synthesized via low-temperature (230 °C) solid-state synthesis followed by cold-press. The high ionic conductivity of $Li_{10}P_3S_{12}I$ at room temperature is only second to $Li_{10}GeP_2S_{12}$, Ge-doped Li_6PS_5I, and the hot-pressed $Li_7P_3S_{11}$. $Li_{10}P_3S_{12}I$ demonstrates much higher stability against Li metal compared with $Li_{10}GeP_2S_{12}$ and $Li_7P_3S_{11}$. The high ionic conductivity, 6.4 mS/cm, of $Li_{10}P_3S_{12}I$ is attributed to the disordered phases and interface with fast Li ion motion. During electrochemical cycling, $Li_{10}P_3S_{12}I$ will partially decompose to form Li_3PS_4 and LiI at electrode−electrolyte interface, and LiI helps to improve interfacial stability.

Acknowledgments

Appendix A. Supplementary data

Supplementary data to this article can be found online at https://do i.org/10.1016/j.ensm.2019.07.047.

References

[1] B. Zhang, R. Tan, L. Yang, J. Zheng, K. Zhang, S. Mo, Z. Lin, F. Pan, Mechanisms and properties of ion-transport in inorganic solid electrolytes, Energy Storage Mater 10 (2018) 139–159.

[2] A. Mauger, M. Armand, C.M. Julien, K. Zaghib, Challenges and issues facing lithium metal for solid-state rechargeable batteries, J. Power Sources 353 (2017) 333–342.

[3] S. Ramakumar, C. Deviannapoorani, L. Dhivya, L.S. Shankar, R. Murugan, Lithium garnets: synthesis, structure, Li$^+$ conductivity, Li$^+$ dynamics and applications, Prog. Mater. Sci. 88 (2017) 325–411.

[4] N.J.J. de Klerk, I. Rosłoń, M. Wagemaker, Diffusion mechanism of Li argyrodite solid electrolytes for Li-ion batteries and prediction of optimized halogen doping: the effect of Li vacancies, halogens, and halogen disorder, Chem. Mater. 28 (2016) 7955–7963.

[5] H.-J. Deiseroth, S.-T. Kong, H. Eckert, J. Vannahme, C. Reiner, T. Zaiß, M. Schlosser, Li$_6$PS$_5$X: a class of crystalline Li-rich solids with an unusually high Li$^+$ mobility, Angew. Chem. 47 (2008) 755–758.

[6] T. Cheng, B.V. Merinov, S. Morozov, W.A. Goddard, Quantum mechanics reactive dynamics study of solid Li-electrode/Li$_6$PS$_5$Cl-electrolyte interface, ACS Energy Lett 2 (2017) 1454–1459.

[7] M. Xuan, W. Xiao, H. Xu, Y. Shen, Z. Li, S. Zhang, Z. Wang, G. Shao, Ultrafast solid-state lithium ion conductor through alloying induced lattice softening of Li$_6$PS$_5$Cl, J. Mater. Chem. A. 6 (2018) 19231–19240.

[8] C. Yu, S. Ganapathy, J. Hageman, L. van Eijck, E.R.H. van Eck, L. Zhang, T. Schwietert, S. Basak, E.M. Kelder, M. Wagemaker, Facile synthesis toward the optimal structure-conductivity characteristics of the argyrodite Li$_6$PS$_5$Cl solid-state electrolyte, ACS Appl. Mater. Interfaces 10 (2018) 33296–33306.

[9] M. Kotobuki, H. Munakata, K. Kanamura, Y. Sato, T. Yoshida, Compatibility of Li$_7$La$_3$Zr$_2$O$_{12}$ solid electrolyte to all-solid-state battery using Li metal anode, J. Electrochem. Soc. 157 (2010) A1076–A1079.

[10] R. Murugan, V. Thangadurai, W. Weppner, Fast lithium ion conduction in garnet-type Li$_7$La$_3$Zr$_2$O$_{12}$, Angew. Chem. 46 (2007) 7778–7781.

[11] X. Han, Y. Gong, K. Fu, X. He, G.T. Hitz, J. Dai, A. Pearse, B. Liu, H. Wang, G. Rubloff, Y. Mo, V. Thangadurai, E.D. Wachsman, L. Hu, Negating interfacial impedance in garnet-based solid-state Li metal batteries, Nat. Mater. 16 (2017) 572–579.

[12] C. Davis, A.L. Pertuit, J.C. Nino, Kinetic analysis of crystallization in Li$_{1.3}$Al$_{0.3}$Ti$_{1.7}$(PO$_4$)$_3$ glass ceramics, J. Am. Ceram. Soc. 99 (2016) 3260–3266.

[13] B. Key, D.J. Schroeder, B.J. Ingram, J.T. Vaughey, Solution-based synthesis and characterization of lithium-ion conducting phosphate ceramics for lithium metal batteries, Chem. Mater. 24 (2012) 287–293.

[14] Y. Zhao, L.L. Daemen, Superionic conductivity in lithium-rich anti-perovskites, J. Am. Chem. Soc. 134 (2012) 15042–15047.

[15] N. Kamaya, K. Homma, Y. Yamakawa, M. Hirayama, R. Kanno, M. Yonemura, T. Kamiyama, Y. Kato, S. Hama, K. Kawamoto, A. Mitsui, A lithium superionic conductor, Nat. Mater. 10 (2011) 682–686.

[16] Y. Kato, S. Hori, T. Saito, K. Suzuki, M. Hirayama, A. Mitsui, M. Yonemura, H. Iba, R. Kanno, High-power all-solid-state batteries using sulfide superionic conductors, Nat. Energy. 1 (2016) 16030.

[17] B.R. Shin, Y.J. Nam, D.Y. Oh, D.H. Kim, J.W. Kim, Y.S. Jung, Comparative study of TiS$_2$/Li-in all-solid-state lithium batteries using glass-ceramic Li$_3$PS$_4$ and Li$_{10}$GeP$_2$S$_{12}$ solid electrolytes, Electrochim. Acta 146 (2014) 395–402.

[18] Y. Seino, T. Ota, K. Takada, A. Hayashi, M. Tatsumisago, A sulphide lithium super ion conductor is superior to liquid ion conductors for use in rechargeable batteries, Energy Environ. Sci. 7 (2014) 627–631.

[19] M.A. Kraft, S. Ohno, T. Zinkevich, R. Koerver, S.P. Culver, T. Fuchs, A. Senyshyn, S. Indris, B.J. Morgan, W.G. Zeier, Inducing high ionic conductivity in the lithium superionic argyrodites Li$_{6+x}$P$_{1-x}$Ge$_x$S$_5$I for all-solid-state batteries, J. Am. Chem. Soc. 140 (2018) 16330–16339.

[20] Z. Zhang, S. Chen, J. Yang, J. Wang, L. Yao, X. Yao, P. Cui, X. Xu, Interface Re-engineering of Li$_{10}$GeP$_2$S$_{12}$ electrolyte and lithium anode for all-solid-state lithium batteries with ultralong cycle life, ACS Appl. Mater. Interfaces 10 (2018) 2556–2565.

[21] P. Bron, B. Roling, S. Dehnen, Impedance characterization reveals mixed conducting interphases between sulfidic superionic conductors and lithium metal electrodes, J. Power Sources 352 (2017) 127–134.

[22] F. Han, Y. Zhu, X. He, Y. Mo, C. Wang, Electrochemical stability of Li$_{10}$GeP$_2$S$_{12}$ and Li$_7$La$_3$Zr$_2$O$_{12}$ solid electrolytes, Adv. Energy Mater. 6 (2016) 1501590.

[23] W.D. Richards, L.J. Miara, Y. Wang, J.C. Kim, G. Ceder, Interface stability in solid-state batteries, Chem. Mater. 28 (2016) 266–273.

[24] M.R. Busche, D.A. Weber, Y. Schneider, C. Dietrich, S. Wenzel, T. Leichtweiss, D. Schröder, W. Zhang, H. Weigand, D. Walter, S.J. Sedlmaier, D. Houtarde, L.F. Nazar, J. Janek, In situ monitoring of fast Li-ion conductor Li$_7$P$_3$S$_{11}$ crystallization inside a hot-press setup, Chem. Mater. 28 (2016) 6152–6165.

[25] P.-H. Chien, X. Feng, M. Tang, J.T. Rosenberg, S. O'Neill, J. Zheng, S.C. Grant, Y.-Y. Hu, Li distribution heterogeneity in solid electrolyte Li$_{10}$GeP$_2$S$_{12}$ upon electrochemical cycling probed by ^{7}Li MRI, J. Phys. Chem. Lett. 9 (2018) 1990–1998.

[26] E. Rangasamy, Z. Liu, M. Gobet, K. Pilar, G. Sahu, W. Zhou, H. Wu, S. Greenbaum, C. Liang, An iodide-based Li$_7$P$_2$S$_8$I superionic conductor, J. Am. Chem. Soc. 137 (2015) 1384–1387.

[27] F. Han, J. Yue, X. Zhu, C. Wang, Suppressing Li dendrite formation in Li$_2$S-P$_2$S$_5$ solid electrolyte by LiI incorporation, Adv. Energy Mater 8 (2018) 1703644.

[28] N.H.H. Phuc, E. Hirahara, K. Morikawa, H. Muto, A. Matsuda, One-pot liquid phase synthesis of (100−x)Li$_3$PS$_4$–xLiI solid electrolytes, J. Power Sources 365 (2017) 7–11.

[29] N.H.H. Phuc, T. Yamamoto, H. Muto, A. Matsuda, Fast synthesis of Li$_2$S–P$_2$S$_5$ –LiI solid electrolyte precursors, Inorg. Chem. Front. 4 (2017) 1660–1664.

[30] S. Wenzel, D.A. Weber, T. Leichtweiss, M.R. Busche, J. Sann, J. Janek, Interphase formation and degradation of charge transfer kinetics between a lithium metal anode and highly crystalline Li$_7$P$_3$S$_{11}$ solid electrolyte, Solid State Ion. 286 (2016) 24–33.

[31] Z. Gan, P.L. Gor`kov, W.W. Brey, P.J. Sideris, C.P. Grey, Enhancing MQMAS of low-γ nuclei by using a high B1 field balanced probe circuit, J. Magn. Reson. 200 (2009) 2–5.

[32] Y. Wang, D. Lu, J. Xiao, Y. He, G.J. Harvey, C. Wang, J.-G. Zhang, J. Liu, Superionic conduction and interfacial properties of the low temperature phase Li$_7$P$_2$S$_8$Br$_{0.5}$I$_{0.5}$, Energy Storage Materials 19 (2019) 80–87.

[33] T. Ohtomo, K. Kawamoto, S. Hama, Y. Kato, Sulfide Solid Electrolyte Glass, Method for Producing Sulfide Solid Electrolyte Glass, and Lithium Solid State Battery, 2015, p. US9172113.

[34] H. Aono, Ionic conductivity of solid electrolytes based on lithium titanium phosphate, J. Electrochem. Soc. 137 (1990) 1023.

[35] C. Bernuy-Lopez, W. Manalastas, J.M. Lopez del Amo, A. Aguadero, F. Aguesse, J.A. Kilner, Atmosphere controlled processing of Ga-substituted garnets for high Li-ion conductivity ceramics, Chem. Mater. 26 (2014) 3610–3617.

[36] M.A. Kraft, S.P. Culver, M. Calderon, F. Böcher, T. Krauskopf, A. Senyshyn, C. Dietrich, A. Zevalkink, J. Janek, W.G. Zeier, Influence of lattice polarizability on the ionic conductivity in the lithium superionic argyrodites Li$_6$PS$_5$X (X = Cl, Br, I), J. Am. Chem. Soc. 139 (2017) 10909–10918.

[37] K. Minami, F. Mizuno, A. Hayashi M. Tatsumisago, Structure and properties of the 70Li$_2$S·(30−x)P$_2$S$_5$·xP$_2$O$_5$ oxysulfide glasses and glass–ceramics, J. Non-Cryst. Solids 354 (2008) 370–373.

[38] S.J. Sedlmaier, S. Indris, C. Dietrich, M. Yavuz, C. Dräger, F. von Seggern, H. Sommer, J. Janek, Li$_4$PS$_4$I: a Li$^+$ superionic conductor synthesized by a solvent-based soft chemistry approach, Chem. Mater. 29 (2017) 1830–1835.

[39] J. Zheng, M. Tang, Y.-Y. Hu, Lithium ion pathway within Li$_7$La$_3$Zr$_2$O$_{12}$-polyethylene oxide composite electrolytes, Angew. Chem. 128 (2016) 12726–12730.